

Article

Effect of Rotary Swaging on Mechanical and Operational Properties of Zn–1%Mg and Zn–1%Mg–0.1%Ca Alloys

Natalia Martynenko ^{1,*}, Natalia Anisimova ^{1,2,3}, Georgy Rybalchenko ⁴, Olga Rybalchenko ¹, Vladimir Serebryany ¹, Mark Zheleznyi ^{1,5,6}, Maria Shinkareva ^{1,3}, Artem Gorbenko ¹, Diana Temralieva ¹, Elena Lukyanova ¹, Andrey Sannikov ^{1,7}, Andrey Koltygin ⁷, Mikhail Kiselevskiy ^{2,3}, Vladimir Yusupov ¹ and Sergey Dobatkin ¹

- ¹ A.A. Baikov Institute of Metallurgy and Materials Science of the Russian Academy of Sciences, Leninsky Prospect, 49, 119334 Moscow, Russia; n_anisimova@list.ru (N.A.); rybalch@mail.ru (O.R.); vserebryany68@gmail.com (V.S.); markiron@mail.ru (M.Z.); m.shinkareva29@mail.ru (M.S.); artemgorbenk@yandex.ru (A.G.); diana4-64@mail.ru (D.T.); helenelukyanova@gmail.com (E.L.); av.sannikov@misis.ru (A.S.); vsyusupov@mail.ru (V.Y.); sdoatkin@imet.ac.ru (S.D.)
- ² N.N. Blokhin National Medical Research Center of Oncology (N.N. Blokhin NMRCO) of the Ministry of Health of the Russian Federation, 115478 Moscow, Russia; kisele@inbox.ru
- ³ Center for Biomedical Engineering, National University of Science and Technology “MISIS”, 119049 Moscow, Russia
- ⁴ P.N. Lebedev Physical Institute of the Russian Academy of Sciences, 119991 Moscow, Russia; rybalchenkogv@lebedev.ru
- ⁵ Department of Physical Materials Science, National University of Science and Technology “MISIS”, 119049 Moscow, Russia
- ⁶ Institute of Innovative Engineering Technologies, Peoples’ Friendship University of Russia (RUDN University), 117198 Moscow, Russia
- ⁷ Department of Casting Technologies and Artistic Processing of Materials, National University of Science and Technology “MISIS”, 119049 Moscow, Russia; misistlp@mail.ru
- * Correspondence: nataliasmartynenko@gmail.com or nata_roug@mail.ru



Citation: Martynenko, N.; Anisimova, N.; Rybalchenko, G.; Rybalchenko, O.; Serebryany, V.; Zheleznyi, M.; Shinkareva, M.; Gorbenko, A.; Temralieva, D.; Lukyanova, E.; et al. Effect of Rotary Swaging on Mechanical and Operational Properties of Zn–1%Mg and Zn–1%Mg–0.1%Ca Alloys. *Metals* **2023**, *13*, 1386. <https://doi.org/10.3390/met13081386>

Academic Editor: Bingshu Wang

Received: 9 July 2023

Revised: 30 July 2023

Accepted: 31 July 2023

Published: 1 August 2023



Copyright: © 2023 by the authors. Licensee MDPI, Basel, Switzerland. This article is an open access article distributed under the terms and conditions of the Creative Commons Attribution (CC BY) license (<https://creativecommons.org/licenses/by/4.0/>).

Abstract: A study of microstructure, phase composition, mechanical properties, corrosion processes, and biocompatibility in vitro of the Zn–1%Mg and Zn–1%Mg–0.1%Ca alloys in an annealed state and after rotary swaging (RS) is presented. Partially recrystallized microstructure is formed in the studied alloys after RS at 200 °C. RS reduces the mass fraction of intermetallic phases in comparison with annealed states of the alloys. RS at 200 °C increases the strength of the Zn–1%Mg and Zn–1%Mg–0.1%Ca alloys up to 248 ± 9 and 249 ± 9 with the growth of ductility up to 10.3 ± 3% and 14.2 ± 0.9%, respectively. The structure after RS at 200 °C does not lead to a change in the corrosion resistance of the studied alloys. However, an increase in the incubation period of the alloys in a growth medium slows down the degradation process due to the formation of a film consisting of degradation products. Rotary swaging does not impair the biocompatibility of the Zn–1%Mg and Zn–1%Mg alloys, maintaining the viability and integrity of blood cells, preventing hemolysis, and ensuring the adhesion and proliferation of osteogenic cells on the surface of samples.

Keywords: zinc alloys; rotary swaging (RS); microstructure; phase composition; mechanical properties; corrosion resistance; biocompatibility in vitro

1. Introduction

According to statistics, fractures of upper and lower limbs account for more than 65% of injuries registered in Russia in 2020 [1]. The period of temporary disability of the patient in case of these injuries can range from several weeks to several months. Reduction in the period of rehabilitation of a patient with fractures of varying degrees of severity is an urgent task during the development of medical devices. One of the most promising options for solving this problem is the development of a new generation of implants for

osteosynthesis that can be dissolved in the body of patients [2–4]. The use of such devices leads to a reduction in the period of treatment of an injury due to the possibility of their complete degradation and, as a result, the disappearance of the necessity for extra surgical intervention. Additionally, the use of biodegradable implants also reduces the risk of developing peri-implant osteoporosis due to the so-called stress shielding effect [5]. In addition, these implants are of particular interest for bone osteosynthesis of children and adolescents with constant bone growth [6].

Zinc and its alloys are some of the most promising materials for the creation of biodegradable osteo-reconstructive implants [7–9]. Firstly, zinc is an essential trace element required for the functioning of the body [10], muscles, and bones [11,12]. It supports the functioning of the central nervous [13] and immune systems [14], has a positive effect on masculine and feminine health [15,16], and much more. Secondly, zinc has good biocompatibility with human and animal cells [17,18]. Finally, the biodegradation rate of zinc is optimal for bones healing and comparable to the rate of recovery of damaged bone tissue [19]. However, a significant disadvantage of zinc as a material for osteosynthesis is its low level of mechanical characteristics and its inability to provide support for the bones of the limbs after fracture. Tong et al. showed that the ultimate tensile strength (UTS) of pure zinc in an as-cast state is 33.6 MPa with a ductility value of 1.2% [20]. Alloying leads to a noticeable increase in the strength characteristics of pure zinc, mainly due to the formation of hardening phases. For example, a gradual increase in the Mg content in binary Zn–Mg alloys from 0 to 0.8 wt.% leads to a monotonic increase in the ultimate tensile strength from ~30 to ~120 MPa [21]. However, an addition of more than 3 wt.% of Mg leads to embrittlement of the alloy and a decrease in the ultimate tensile strength to ~90 MPa [22]. In the case of Zn–Cu alloys, it was shown that an increase in the Cu content up to 4 wt.% leads to an increase in UTS to 105 MPa [23]. Huang et al. also showed that a combination of UTS and ductility equal to ~158 MPa and ~6.3%, respectively, can be obtained after the addition of 2 wt.% Al to cast Zn [24]. However, even this level of mechanical characteristics is not sufficient for the successful use of zinc alloys as a material for creating implants for osteosynthesis [25]. Therefore, the necessity for improvement in the mechanical characteristics of Zn alloys appears. Plastic deformation is an optimal way to perform it.

Rotary swaging (RS) is a popular deformation method due to its simplicity, industrial applicability, and low cost [26]. Recently, this deformation method has been widely used for processing bioresorbable medical alloys based on Mg [27–29], which, like Zn, is a metal with a hexagonal close-packed (hcp) lattice. In these studies, it was shown that RS makes it possible to effectively refine the microstructures of hcp metals, increasing their strength properties. The microstructure caused by RS can both increase the degradation rate of alloys [30] and reduce it [31]. In addition, the degradation rate can remain unchanged due to the formation of a mixed microstructure, including both ultrafine grains and deformation twins [32]. At the same time, the effect of RS on the structure and properties of medical zinc alloys has not been practically studied yet. However, the research shows the competitive advantage of this type of processing [33]. Therefore, the purpose of this work was to study the effect of rotary swaging at elevated temperatures on the change in the structure and phase composition of Zn–1%Mg and Zn–1%Mg–0.1%Ca alloys, promising for use in medicine. It is expected that the structure and phase changes caused by RS can increase the mechanical characteristics of the alloys. It is also anticipated that the suppression of twinning in the process of high-temperature deformation will not cause an increase in the degradation rate. In addition, the effect of RS on the biocompatibility of the alloys by evaluating hemolysis of red blood cells and cell viability after co-incubation with the alloys, as well as cell colonization of their surface was investigated.

2. Materials and Methods

In this work, the Zn–1%Mg and Zn–1%Mg–0.1%Ca alloys were studied. The alloys were melted in an induction furnace in a clay–graphite crucible under air conditions.

The melt was poured into a steel mold preheated to 150 °C. The nominal composition of alloys determined using chemical methods was Zn– ~0.98 wt.% Mg and Zn– ~1.06 wt.% Mg– ~0.12 wt.% Ca. The alloys were annealed at 340 °C for 20 h with cooling in water. This condition was referred to as «initial state» or «IS». The rods 19 mm in diameter and 150 mm in length were cut from initial billets to conduct the deformation process. RS was carried out with a gradual decrease in temperature up to 200 °C with a decrease in the diameter of the rods from 19 to 6 mm (Figure 1). RS was carried out on a rotary swaging machine RKM 2129.02 (UZM, Sverdlovsk, USSR). A frequency and a striker travel were 1920 min⁻¹ and 3 mm, respectively. It means that eight strokes of the strikers corresponded to one rotation of the rod around its axis. The rods were heated at a deformation temperature for 45 min before the first pass of RS. Then, the rods were heated for 15 min before every change of the strikers. More details were described in [34]. A study of the alloy after RS was carried out with a total deformation degree equal to 1.28 and 2.31.

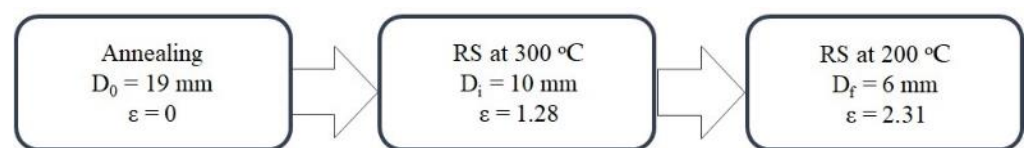


Figure 1. The RS processing regime employed (D denotes the diameter of the billet, ε ($\varepsilon = \ln(A_0/A_f)$ where A_0 and A_f are the initial and the final cross-section areas of the billets, respectively) denotes the deformation degree).

The microstructure was studied using optical microscopy using an M-24 microscope (Reichert, Vienna, Austria). The study of the microstructure of the alloys after deformation was carried out in the longitudinal direction (parallel to the RS direction). The average grain size was calculated using Image Expert Professional 3 software (Version 3, Nexsys, Moscow, Russia). The grain size was measured using the method of random sections. At least 300 grains were measured to calculate the average grain size. The phase analysis of the alloys after RS was carried out on a Bruker D8 Advance diffractometer (Bruker, Karlsruhe, Germany). The research was performed using CuK α radiation ($\lambda = 1.54 \text{ \AA}$). The results were processed according to the Rietveld method. Bruker DIFFRAC.EVA™ (Bruker, Karlsruhe, Germany), DIFFRAC.TOPAS™ (Bruker, Karlsruhe, Germany), and ICDD PDF-2 2020™ (Newtown Square, PA, USA) software was used for this purpose. The mechanical characteristics of the alloys were investigated in the longitudinal direction for alloys after deformation on an Instron 3382 testing machine (Instron, High Wycombe, UK). The studies were carried out at room temperature on flat samples with a working length of 5.75 mm and a cross-section of 2 × 1 mm.

The texture was studied for the Zn1%Mg and Zn1%Mg0.1%Ca alloys after annealing and RS at 200 °C (cross direction). It was analyzed using a DRON-7 X-ray texture diffractometer (SPE “Burevestnik”, St. Petersburg, Russia) in CoK α radiation in the reflection mode by recording five incomplete pole figures {00.2} {10.0}, {10.1}, {10.2}, {11.0}. A maximum tilt angle (α_{\max}) was 70° and a step of angles α and β (0–360°) was 5°. Here, α and β are the radial and azimuth angles on the pole figure. The orientation distribution function (ODF) was calculated from the measured pole figures using the method of approximation using a large number (1000) of Gaussian normal distributions [35].

The corrosion resistance of the alloys was evaluated using the method of potentiodynamic polarization at room temperature in 0.9% NaCl solution. The studies were carried out using an SP-300 potentiostat (Bio-Logic SAS, Seyssinet-Pariset, France). The samples were placed in a flat PAR cell (Ametek Instruments, Oak Ridge, TN, USA) with a “three-electrode configuration”: working electrode (sample), Ag/AgCl reference electrode, and counter electrode from Pt grid. At least six scans were performed for each state of the alloys. The scanning rate was 1 mV/s. Corrosion parameters were calculated using the EC-Lab

program (BioLogic, Seyssinet-Pariset, France) in accordance with [36]. The corrosion rate (CR) was calculated using the corrosion current density (i_{corr}) as described in [36,37]:

$$CR = \frac{3.27 * 10^{-3} * i_{corr} * EW}{\rho * S}$$

where CR is the corrosion rate (mm/year), i_{corr} is the corrosion current density, $\mu\text{A}/\text{cm}^2$; EW is the equivalent weight, g/eq; ρ —alloys density, g/cm^3 .

Square-shaped samples with dimensions of $5 \times 5 \times 2$ mm (length \times width \times thickness) were used for biological studies in vitro and the immersion tests. Three samples of the same alloy's state were used for each test. Samples were sterilized via immersion in 70% ethanol for 2 h, and then they were dried under sterile conditions.

Prior to degradation rate studies, the samples were weighed on a Sartorius M2P Micro Balances Pro 11 electronic balance (Data Weighing Systems, Inc., Wood Dale, IL, USA; three digits per 1 mg). Next, the samples were placed in separate wells of a 24-well plate (Thermo Scientific, Waltham, MA, USA) with 2 mL of a complete growth medium based on Eagle's Minimum Essential Medium (Sigma, Welwyn Garden City, UK) supplemented with 2 mM L-glutamine, 5% fetal bovine serum (PanEco, Moscow, Russia), and 50 U/mL penicillin/streptomycin. The samples were immersed in a growth medium at 37 °C in an atmosphere of 5% carbon dioxide for 1 and 30 days. The medium was changed every 2 days. At the end of the incubation period, the samples were cleaned in a mixture of $(\text{NH}_4)_2\text{S}_2\text{O}_8$ and distilled water to remove degradation products. After cleaning, sterile-dried samples were reweighed. The degradation rate of the studied alloys was calculated according to the procedure described in [38]. The study of the surface of the samples after immersion tests before cleaning was carried out on a JSM-7001F scanning electron microscope (JEOL; Tokyo, Japan).

To assess the effect on hemolysis, red blood cells (RBC) extracted from the peripheral blood of a Balb/c mouse (weight 20–22 g) were used. For this purpose, blood stabilized with 10 IU of heparin (Belmedpreparaty, Minsk, Belarus) was suspended in Hank's solution (PanEco, Moscow, Russia) and centrifuged at 3000 rpm for 5 min to isolate RBC. Then, the RBCs were washed three times with Hank's solution.

A total of 1.5 mL of RBC suspension with a concentration of 4,420,000 cells per 1 mL was added to wells with the samples for hemolysis assay. Samples with cell suspension were incubated at 37 °C in an atmosphere consisting of 5% carbon dioxide. After 2 h, 300 μL of cell suspension was taken from each well and centrifuged at 3000 rpm for 5 min. Then, 100 μL of the supernatant was taken from each sample into doublets and transferred to a 96-well plate (SPL Life Science, Pocheon, Republic of Korea). Finally, the optical density (OD) was measured using a Spark plate reader (Tecan, Zürich, Switzerland) at 540 nm.

Suspension of cells treated with 1% Triton X-100 (PanReac, AppliChem, Barcelona, Spain) was used as a positive control (*Pos. control*). A suspension of RBC, which was incubated without samples, was used as a negative control (*Neg. control*). Hemolysis results were calculated using the formula:

$$\text{Hemolysis (\%)} = \frac{OD (\text{Alloy}) - OD (\text{Neg. control})}{OD (\text{Pos. control}) - OD (\text{Neg. control})} \times 100$$

To assess the effect of alloys on cell viability, mouse peripheral blood mononuclear cells (PBMC) were used. In order to perform this, the blood was stabilized with heparin, diluted twice with Hank's solution, carefully layered on ficoll (PanEco, Moscow, Russia), and centrifuged at 1500 rpm for 20 min. Then, the interfacial ring was carefully removed and washed three times using Hank's solution at 1100 rpm for 5 min. PBMC were suspended in a complete growth medium to a concentration of 300,000 cells per 1 mL. A total of 1.5 mL of PBMC suspension was added to the samples and incubated for 24 h at 37 °C in an atmosphere consisting of 5% carbon dioxide. At the end of the incubation, 300 μL of the supernatant was taken and centrifuged at 1000 rpm for 5 min. The integrity of the cell

membrane was analyzed by assessing the release of lactate dehydrogenase (LDH) using the Lactate Dehydrogenase Activity Assay Kit (Sigma-Aldrich, St. Louis, MI, USA) according to the manufacturer's instructions. Optical density measurements were made in a 96-well plate using a plate reader at 450 nm. As a control, PBMC incubated under similar conditions in the absence of samples was used. *Cell viability* was calculated using the formula:

$$\text{Cell viability (\%)} = \frac{OD (\text{Alloy}) - OD (\text{Medium})}{OD (\text{Control}) - OD (\text{Medium})} \times 100$$

Cell colonization was assessed using multipotent mesenchymal stromal cells (MMSCs) obtained from mouse femur bone marrow. The bone marrow was isolated from the femurs that were removed from the mice after euthanasia. The bone marrow cells were suspended in a complete growth medium. Further, MMSC culture was generated from the isolated cells in Mesenchymal Stem Cell Expansion Media (R&D Systems, Minneapolis, MN, USA). The cells of passage 3 with the CD45[−]CD34⁺CD105⁺ phenotype, which was determined via flow cytometry on a NovoCyte instrument (Acea, San Diego, CA, USA) using Anti-mouse CD45, Anti-mouse CD34, Anti-mouse CD105 antibodies (eBioscience, Thermo Scientific, Waltham, MA, USA), conjugated with fluorochromes were used for studies. The concentration of living cells was determined using a Luna-II cell analyzer (Logos Biosystems, Gyeonggi-do, Republic of Korea) in accordance with the manufacturer's instructions. Cells were concentrated in a complete growth medium. The cell concentration was 80,000 living cells per 1 mL. A total of 15 μ L of the cell suspension was seeded on the dry surface of the alloy samples and incubated for 30 min at 37 °C in an atmosphere consisting of 5% carbon dioxide. Then, 2 mL of complete cell medium was carefully added to the wells and incubated for 15 days under the described above conditions. The medium was changed every 2 days. The test result was evaluated via the change in cell viability after staining with AlamarBlue (Invitrogen, Thermo Scientific, Waltham, MA, USA) according to the manufacturer's instructions. The optical density was measured using a plate reader at 570 nm. The cells incubated under the same conditions without samples were used as a control. The result was calculated using the formula:

$$\text{Cell colonization (\%)} = \frac{OD (\text{Alloy}) - OD (\text{Medium})}{OD (\text{Control}) - OD (\text{Medium})} \times 100$$

In addition, to visualize the cells on the surface of the samples, staining was used with the Live/Dead kit (Invitrogen, Thermo Scientific, Waltham, MA, USA) and analyzed using a Lionheart FX microscope (BioTek, Shoreline, DC, USA).

The results of the studies are presented as the mean \pm standard deviation (Mean \pm SD). Comparison between the two groups was performed using Student's *t*-test. Differences were considered statistically significant at $p < 0.05$.

3. Results and Discussion

Figure 2 shows the results of a study of the microstructure of alloys in the annealed state and after RS at 300 °C and 200 °C. The structure of the alloys after annealing consists of α -Zn grains surrounded by a thick phase layer. As shown earlier, this phase is a mixture of Mg₂Zn₁₁ and MgZn₂ phases [39]. In addition, the inclusions with a regular geometric shape are observed in the structure of the Zn-1%Mg-0.1%Ca alloy. They were previously identified as CaZn₁₁ and CaZn₁₃ phases [39]. The average grain size of α -Zn was 36 \pm 2 and 30 \pm 3 μ m for Zn-1%Mg and Zn-1%Mg-0.1%Ca alloys, respectively (Figure 2a,b).

RS leads to microstructure refinement and elongation of α -Zn grains and grain-boundary phase along the deformation direction. The grains with an average width of 25 \pm 2 and 20 \pm 1 μ m are formed after RS at 300 °C in the Zn-1%Mg and Zn-1%Mg-0.1%Ca alloys, respectively (Figure 2c,d). A further decrease in the deformation temperature leads to the formation of the alloys of a mixed fine microstructure. This microstructure includes the remains of grains elongated along the RS direction, recrystallized grains, and inclusions

of magnesium and calcium phases comparable in size to recrystallized grains (Figure 2e,f). The average size of the recrystallized grains in this case was 7 ± 0.4 and 10 ± 0.6 μm in Zn-1%Mg and Zn-1%Mg-0.1%Ca alloys, respectively.

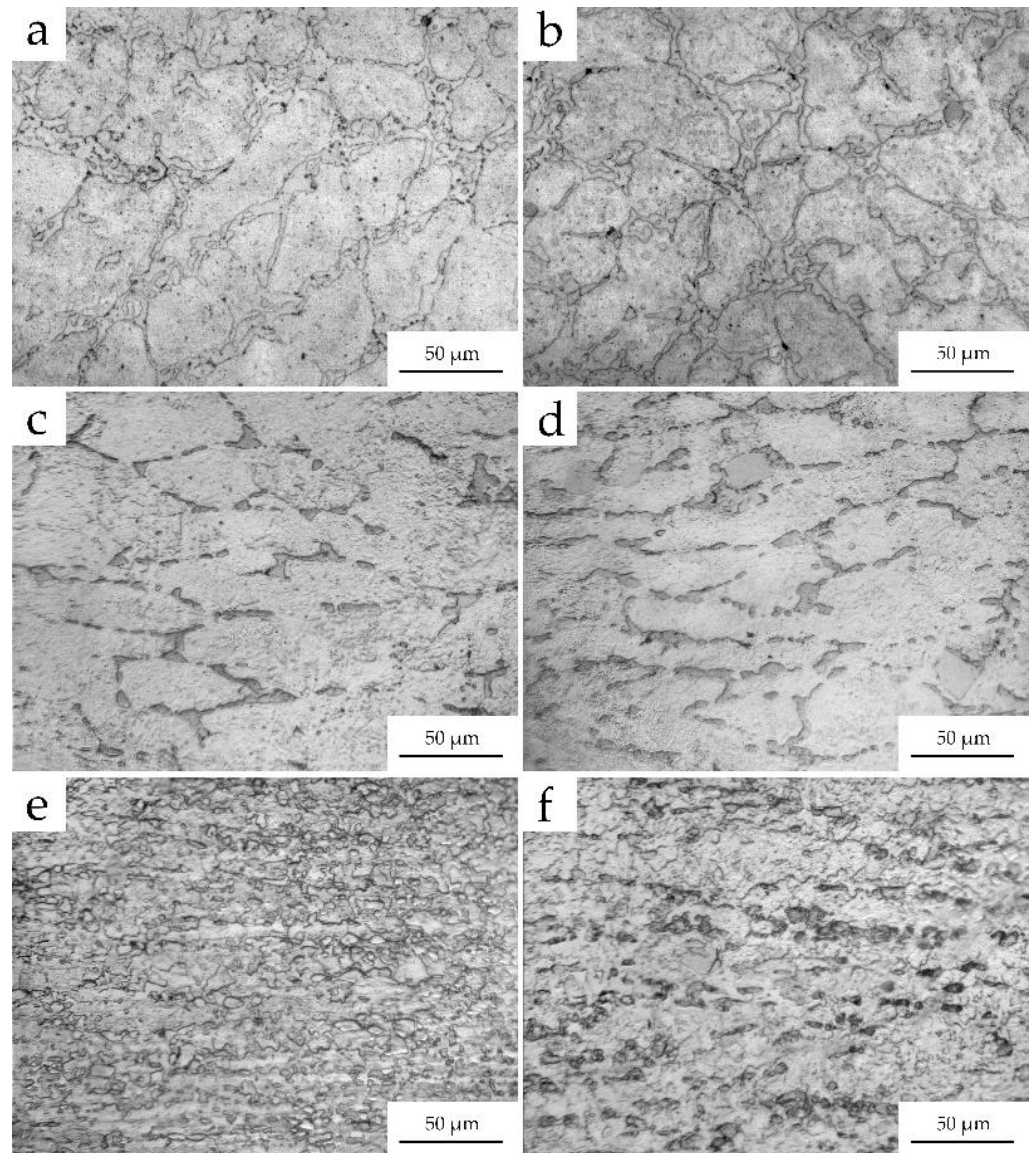


Figure 2. Microstructure of the Zn-1%Mg (a,c,e) and Zn-1%Mg-0.1%Ca (b,d,f) alloys in the annealed state (a,b) and after RS at 300 °C (c,d) and 200 °C (e,f).

Figure 3 and Table 1 show the results of X-ray diffraction analysis of alloys after RS at 300 °C and 200 °C. In our previous study, it was shown that three phases are formed in the annealed Zn-1%Mg alloy: α -Zn, $\text{Mg}_2\text{Zn}_{11}$, and MgZn_2 [40]. In the case of the Zn-1%Mg-0.1%Ca alloy, additional phases of CaZn_{11} and CaZn_{13} were found [39]. The phase composition of the alloys does not change after RS at both temperatures (Figure 3). However, it should be noted that partial dissolution of both Mg- and Ca-containing phases occurs during the RS process. This process is accompanied by an increase in the mass fraction of α -Zn.

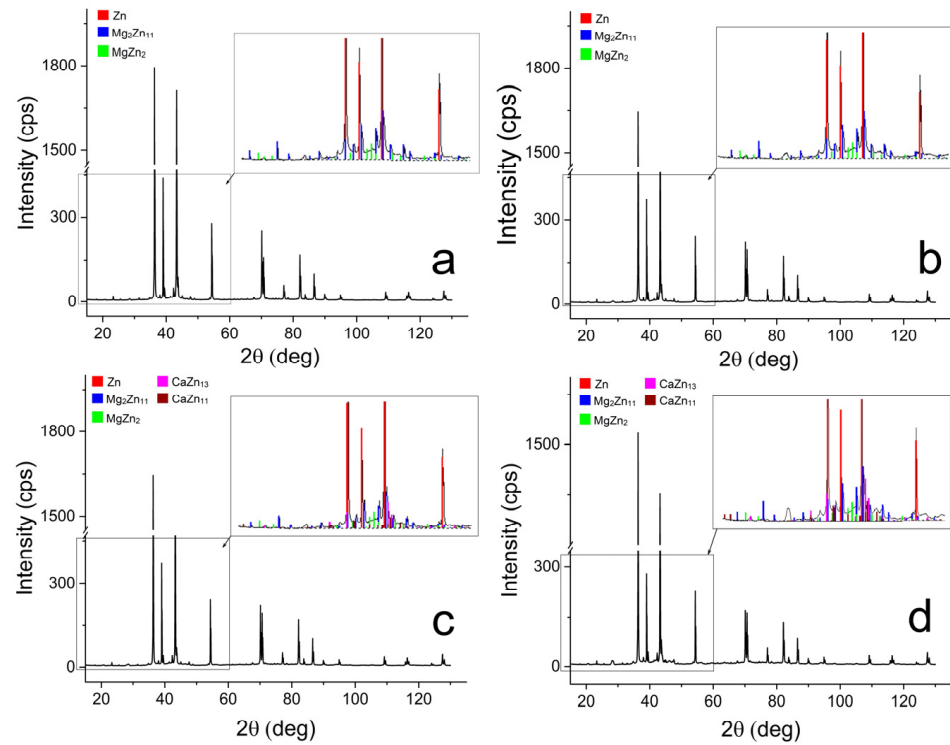


Figure 3. X-ray analysis of the Zn–1%Mg (a,c) and Zn–1%Mg–0.1%Ca (b,d) alloys after RS at 300 °C (a,b) and 200 °C (c,d).

Table 1. Quantitative phase analysis (Rietveld method) of the Zn–1%Mg and Zn–1%Mg–0.1%Ca alloys before and after RS.

State	State	Phase	Mass Fraction, wt. %	Crystallite Size, nm	
Zn–1%Mg	Annealing *	α -Zn	89.7 ± 2.2	913 ± 109	
		Mg ₂ Zn ₁₁	7.3 ± 1.6	619 ± 378	
		MgZn ₂	3.0 ± 0.8	212 ± 64	
	RS at 300 °C	α -Zn	95.4 ± 2.9	954 ± 153	
		Mg ₂ Zn ₁₁	3.5 ± 2.7	516 ± 369	
		MgZn ₂	1.0 ± 0.6	35 ± 23	
	RS at 200 °C	α -Zn	96.0 ± 3.5	952 ± 182	
		Mg ₂ Zn ₁₁	2.9 ± 1.3	636 ± 356	
		MgZn ₂	1.1 ± 0.7	92 ± 29	
Zn–1%Mg–0.1%Ca	Annealing *	α -Zn	72.9 ± 9.3	804 ± 133	
		Mg ₂ Zn ₁₁	5.9 ± 1.3	549 ± 408	
		MgZn ₂	8.9 ± 1.4	356 ± 119	
		CaZn ₁₃	6.0 ± 2.0	635 ± 120	
		CaZn ₁₁	6.3 ± 1.9	194 ± 139	
	RS at 300 °C	α -Zn	94.8 ± 7.2	945 ± 472	
		Mg ₂ Zn ₁₁	2.0 ± 0.6	835 ± 667	
		MgZn ₂	0.5 ± 0.3	163 ± 116	
		CaZn ₁₃	1.7 ± 0.8	189 ± 121	
		CaZn ₁₁	1.0 ± 0.5	101 ± 56	
		α -Zn	95.4 ± 7.2	954 ± 557	
		RS at 200 °C	Mg ₂ Zn ₁₁	1.3 ± 0.6	890 ± 636
			MgZn ₂	0.7 ± 0.4	189 ± 136
			CaZn ₁₃	1.5 ± 0.8	292 ± 209
			CaZn ₁₁	1.1 ± 0.5	105 ± 59

* Results of quantitative phase analysis (mass fraction) of annealed alloys were presents in [39,40].

Table 2 and Figure 4 present the results of a study of the mechanical characteristics of Zn–1%Mg and Zn–1%Mg–0.1%Ca alloys before and after RS. A slight increase in the ultimate tensile strength (UTS) and ductility occurred in the Zn–1%Mg alloy after RS at 300 °C. However, a decrease in the RS temperature up to 200 °C and an increase in the deformation degree leads to a significant increase in UTS (up to 248 ± 9 MPa) and ductility (up to $10.3 \pm 2.0\%$).

Table 2. Mechanical properties of the Zn–1%Mg and Zn–1%Mg–0.1%Ca alloys in the initial state and after RS.

Alloy	State	YS, MPa	UTS, MPa	El, %
Zn–1%Mg	Annealing	153 ± 7	156 ± 3	0.2 ± 0.04
	RS at 300 °C	157 ± 14	179 ± 9	2.2 ± 1.0
	RS at 200 °C	223 ± 23	248 ± 9	10.3 ± 2.0
Zn–1%Mg–0.1%Ca	Annealing	135 ± 13	154 ± 5	0.4 ± 0.1
	RS at 300 °C	174 ± 13	195 ± 17	1.1 ± 0.3
	RS at 200 °C	215 ± 13	246 ± 9	14.2 ± 0.9

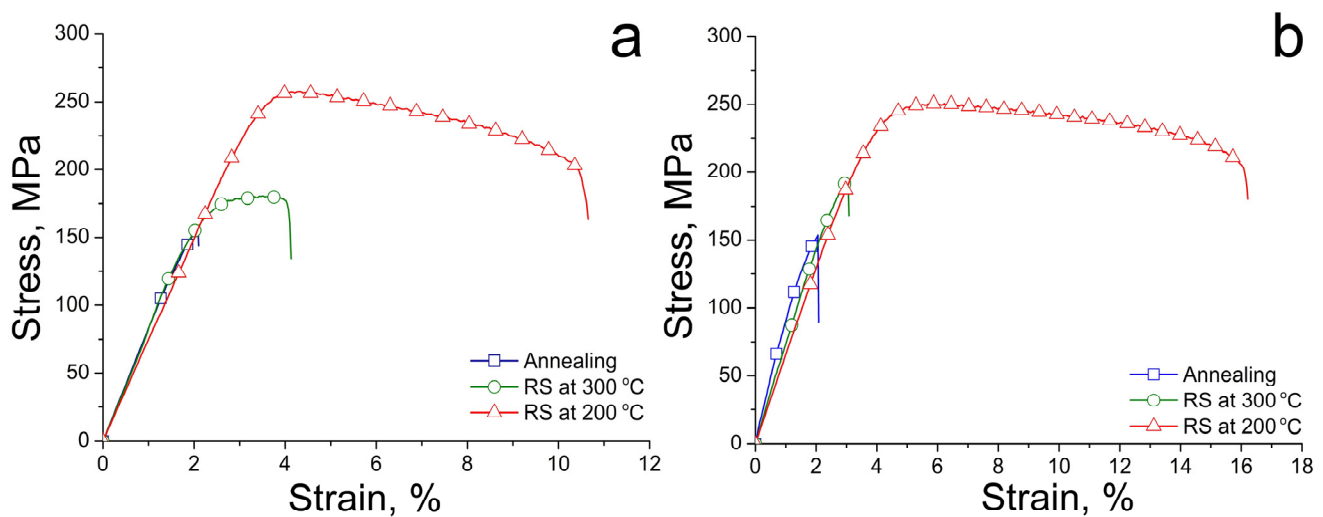


Figure 4. Engineering stress–strain response of the Zn–1%Mg (a) and Zn–1%Mg–0.1%Ca (b) alloys before and after RS.

A gradual increase in strength and ductility also happens in the Zn–1%Mg–0.1%Ca alloy after RS. Thus, the strength of the alloy after RS at 200 °C increased from 154 ± 5 to 246 ± 9 MPa. In addition, a significant increase in ductility from $0.4 \pm 0.1\%$ to $14.2 \pm 0.9\%$ was observed in the alloy.

The increase in strength characteristics is mainly caused by a decrease in grain size during deformation. Thus, a slight refinement of the microstructure after RS at 300 °C causes only a small increase in strength. At the same time, YS and UTS of alloys are increased significantly after RS at 200 °C, which correlates with a strong grain refinement. In this case, the increase in ductility is apparently associated with two factors. The first is connected with the decrease in the proportion of grain-boundary phases and the change in their shape and location. The second arises from the changes in the texture of the alloys. The last factor often accompanies the deformation of zinc, leading to an increase in ductility. Lou et al. showed that the texture transformation of the Zn–0.2Mg–0.8Mn (wt.%) alloy during indirect extrusion at different temperatures significantly increased elongation from 12% to 33% [41]. At the same time, Wang et al. showed that activation of non-basal texture components increased the ductility of Zn–Mg–Mn alloys from 23% to 30% [42].

Therefore, the texture of alloys after annealing and RS at 200 °C was studied to evaluate the contribution of texture to the increase in their ductility. The analysis of the results of this study is presented in Figure 5. The texture of the Zn–1%Mg alloy after annealing is characterized by a dispersed basal orientation (Figure 5a). Further scattering of this basal texture (see Figure 5b) occurs after RS at 200 °C due to dynamic recrystallization caused by warm deformation. The texture of the Zn–1%Mg–0.1%Ca alloy after annealing (Figure 5c) and RS (Figure 5d) is close to the texture of the Zn–1%Mg alloy and is characterized by a dispersed basal component. The difference is observed in the annealed state of the alloy, where the scattering of the basal component is greater than in the Zn–1%Mg alloy. The main reason for the appearance of a dispersed basal component after RS is likely associated with the process of dynamic recrystallization.

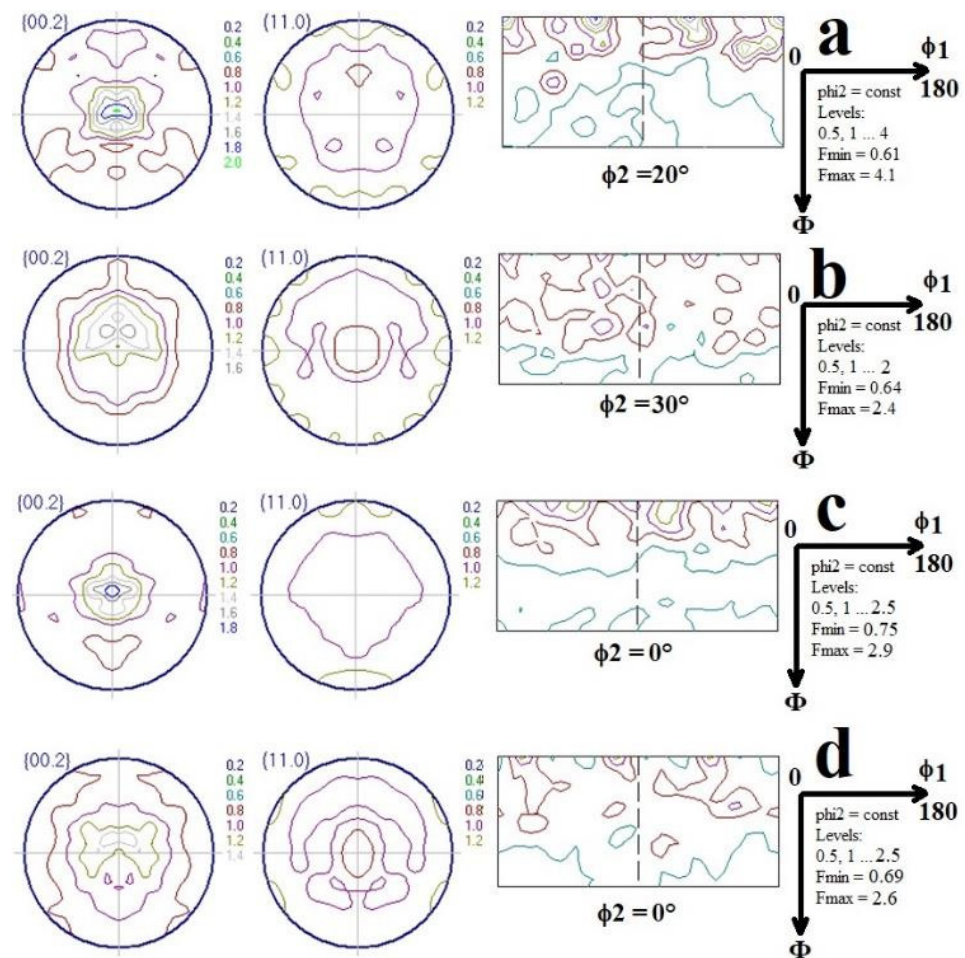


Figure 5. {00.2} and {11.0} pole figures and ODF section of the Zn–1%Mg (a,b) and Zn–1%Mg–0.1%Ca (c,d) alloys after annealing (a,c) and RS at 200 °C (b,d).

Based on the obtained data, it can be concluded that RS does not lead to a significant change in the texture of the studied alloys. Therefore, its significant contribution to the increase in ductility can be excluded. Apparently, the structural phase changes that occur in alloys after RS are the probable reason for the increase in the ductility of alloys in this case. Firstly, the decrease in the mass fraction of phases can affect elongation. Secondly, changes in the location of these phases from a continuous network along the α -Zn grain boundary to individual lines of small, round inclusions have a beneficial effect. In our case, the mass fraction of Mg- and Ca-containing phases decreases after RS at 300 °C (Table 1). However, the location of these phases is still similar to the location of phases in alloys in the initial state. On the other hand, the mass fraction of phases in alloys after RS at 200 °C does not decrease in comparison with RS at 300 °C, but their location and shape change.

Probably, the shape and distribution of the phases have the greatest effect on ductility. In addition, partial dynamic recrystallization caused by warm RS can also improve ductility. It was previously reported that continuous dynamic recrystallization in Zn–Mg alloys is possible in a wide range of deformation temperatures, including even below-freezing temperatures [43,44]. At the same time, Jarzebska et al. demonstrated a tremendous effect of continuous dynamic recrystallization on the ductility of Zn–1Cu alloy [45].

Figure 6 and Table 3 show the results of studies of electrochemical corrosion and weight loss (immersion tests) of the alloys after 1 and 30 days of incubation.

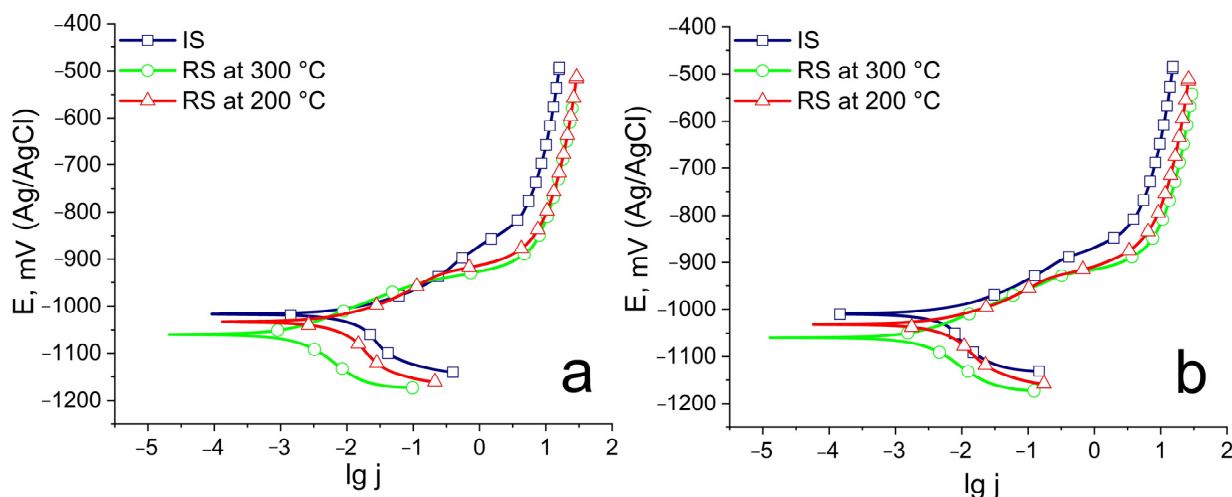


Figure 6. Polarization curves (Ag/AgCl electrode) in 0.9% NaCl solution of the Zn–1%Mg (a) and Zn–1%Mg–0.1%Ca (b) alloys before and after RS.

Table 3. Corrosion resistance and degradation rate (DR in mm/y) of the Zn–1%Mg and Zn–1%Mg–0.1%Ca alloys in the initial state and after RS.

Alloy	State	E, mV (Ag/AgCl)	I, $\mu\text{A}/\text{cm}^2$	CR, mm/y	DR, mm/y	
					1 Day	30 Days
Zn–1%Mg	Annealing	-1018 ± 8	20.7 ± 7.9	0.30 ± 0.17	0.25 ± 0.02	0.12 ± 0.02
	RS at 300 °C	-1059 ± 20	10.5 ± 1.8	0.19 ± 0.05	-	-
	RS at 200 °C	-1029 ± 15	16.7 ± 1.7	0.26 ± 0.05	0.28 ± 0.01	0.11 ± 0.01
Zn–1%Mg–0.1%Ca	Annealing	-1009 ± 5	10.7 ± 4.4	0.20 ± 0.08	0.25 ± 0.01	0.20 ± 0.02
	RS at 300 °C	-1055 ± 18	13.2 ± 2.6	0.22 ± 0.06	-	-
	RS at 200 °C	-1033 ± 16	15.3 ± 3.2	0.25 ± 0.07	0.31 ± 0.03	0.25 ± 0.01

RS at 300 °C leads to a significant decrease in the corrosion potential of both alloys, which indicates an increase in the tendency of alloys to electrochemical corrosion. At the same time, RS at 300 °C also leads to a decrease in the corrosion current density, which means a reduction in the rate of electrochemical corrosion. A decrease in the deformation temperature to 200 °C increases both the corrosion potential and the corrosion current density relative to the state deformed at 300 °C. However, it should be noted that the corrosion parameters obtained for alloys after RS at 200 °C do not differ significantly from the values obtained for the initial state of the alloys (Table 3). Based on the results of the study of mechanical and corrosion properties, it was decided to carry out further investigations on alloys in the initial state and after RS at 200 °C.

The results of immersion tests, in general, are in good agreement with the results of the study of electrochemical corrosion. Thus, it was shown that RS at 200 °C does not lead to a change in the degradation rate relative to the initial state of the alloy, neither after 1 day nor after 30 days of incubation (Table 3). In the Zn–1%Mg alloy, the degradation rate after

1 day of incubation is 0.25 ± 0.02 mm/y and 0.28 ± 0.01 mm/y before and after deformation, respectively. In the Zn-1%Mg-0.1%Ca alloy, these values are 0.25 ± 0.01 mm/y and 0.31 ± 0.03 mm/y, respectively. An increase in the sample incubation period leads to a slowdown in the degradation rate for both states of the alloys. In the case of the Zn-1%Mg alloy, the degradation rate decreased by a factor of 2 (0.12 ± 0.02 mm/y and 0.11 ± 0.01 mm/y before and after deformation, respectively). At the same time, only a slight decrease in the degradation rate to 0.20 ± 0.02 mm/y and 0.31 ± 0.01 mm/y occurred in the Zn-1%Mg-0.1%Ca alloy before and after deformation, respectively. The corrosion rate (CR) calculated from the electrochemical plots is in good agreement with the data obtained in immersion tests (DR).

Figure 7 shows the results of studying the sample surface of both alloys after immersion tests for 30 days in an environment based on the Eagle's Minimum Essential Medium.

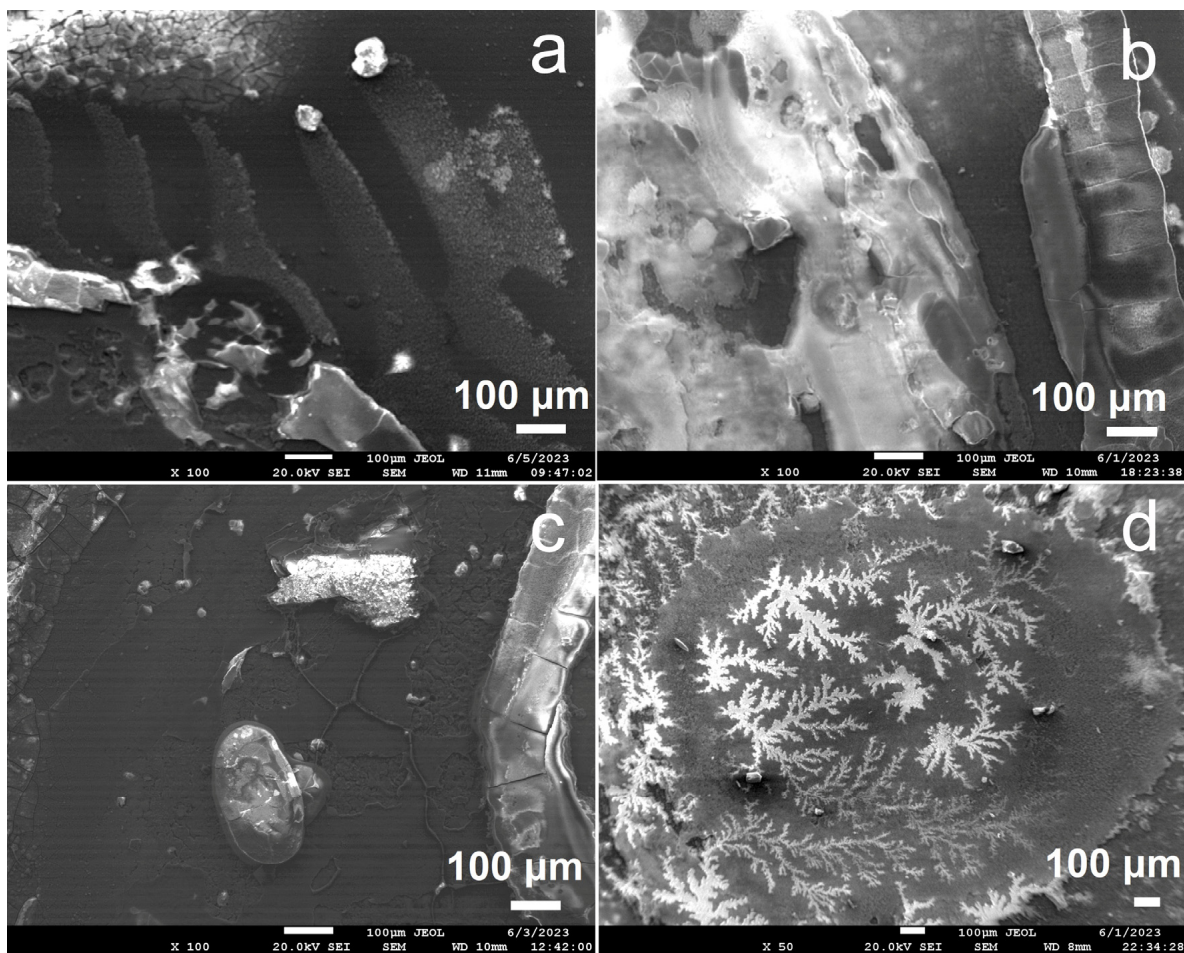


Figure 7. SEM images of degraded surfaces of the annealed (a,c) and RS-treated (b,d) Zn-1%Mg (a,b) and Zn-1%Mg-0.1%Ca (c,d) alloys after immersion tests for 30 days in the Eagle's Minimum Essential Medium.

The layer of degradation products formed on the surface of all samples is ununiform. A zone with a dense film of degradation products on the surface is observed. It protects the sample from further degradation. However, zones that practically are not covered by degradation products are also discovered. There, the degradation process goes faster. The formation of zones with a denser layer of degradation products is probably associated with the presence of less corrosion-resistant magnesium and calcium phases. The presence of these phases leads to the beginning of micro galvanic corrosion between the more resistant zinc matrix (cathode) and phases (anode) [46]. At the same time, the formation of the film apparently leads to inhibition of the degradation process with an increase in the

incubation period, which affects the value of the degradation rate. However, the formation of inhomogeneous film leads to a decrease in degradation rate. It should be noted that the film formed on the surface of the Zn–1%Mg alloy samples is denser compared to the Zn–1%Mg–0.1%Ca alloy (Figure 7). Apparently, this is the reason for the stronger deceleration of the degradation process for the Zn–1%Mg alloy. To assess the composition of the formed degradation products, SEM elemental scanning of the surface of the samples was carried out (Figures 8 and 9).

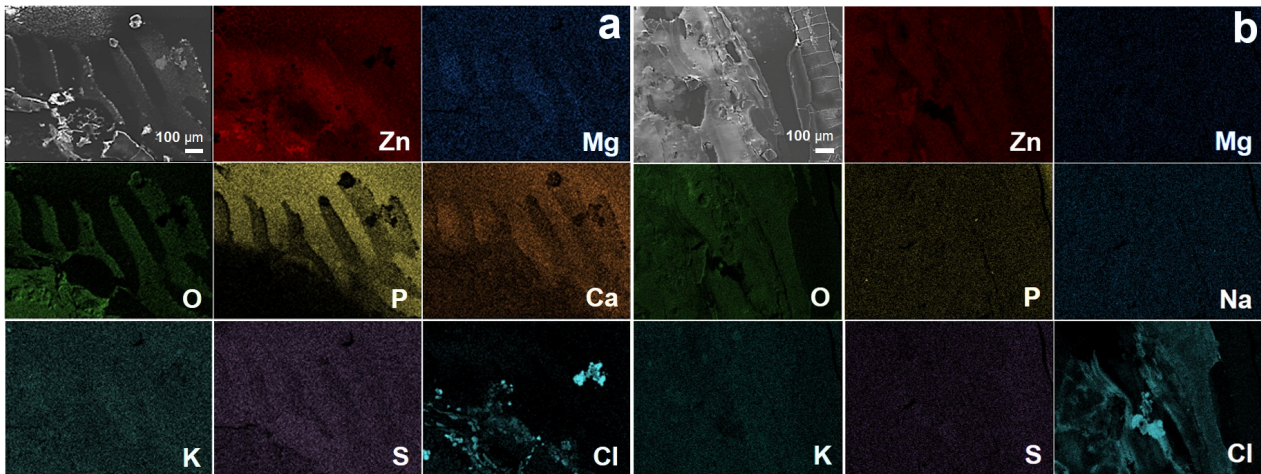


Figure 8. Elemental mapping of annealed (a) and RS-treated (b) Zn–1%Mg alloy after immersion tests.

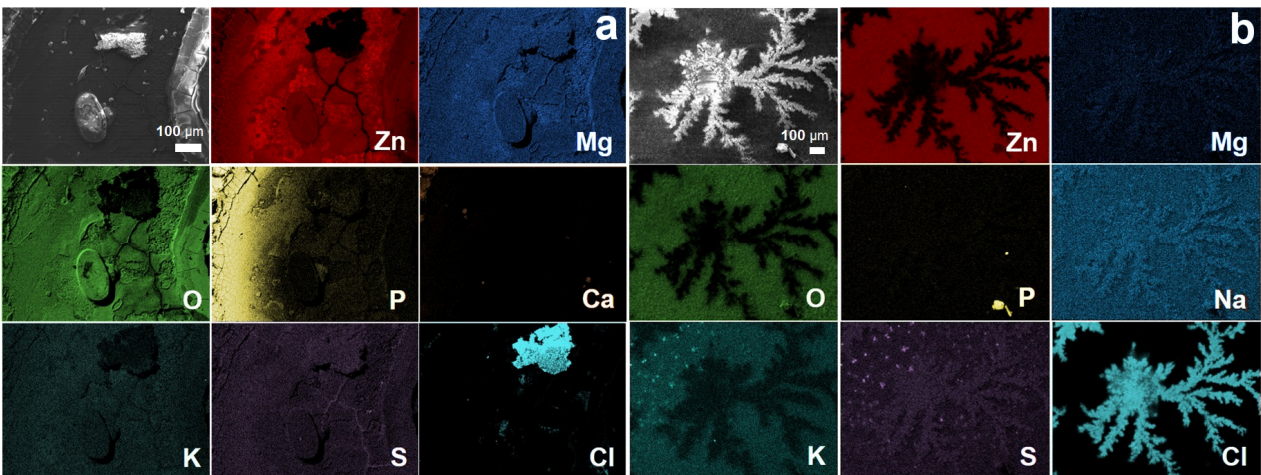


Figure 9. Elemental mapping of annealed (a) and RS-treated (b) Zn–1%Mg–0.1%Ca alloy after immersion tests.

The results of the study of the composition of the alloy degradation products showed that the composition of the degradation products also contained such elements as O, P, Na, K, S, and Cl in addition to the main components of the alloy (Zn, Mg, and Ca). The presence of these elements is caused by the composition of the immersive medium [47].

The presence of a large amount of chlorine in the degradation products in the form of clusters on the surface of the samples also should be noted. Apparently, they are mostly NaCl aggregations, which are the basis of the Eagle’s Minimum Essential Medium culture medium [47]. The SEM-EDS analysis of degradation products carried out in areas of Cl accumulation confirms this hypothesis (Figure 10 and Table 4). The SEM-EDS analysis of Zn–1%Mg–0.1%Ca alloy after RS showed that there are two types of zones on the surface of the samples after incubation in Eagle’s Minimum Essential Medium. Zinc oxides ZnO are predominantly formed in the first case (spectrums 1 and 4). The NaCl compounds (spectrums 2 and 3) appear in the second case.

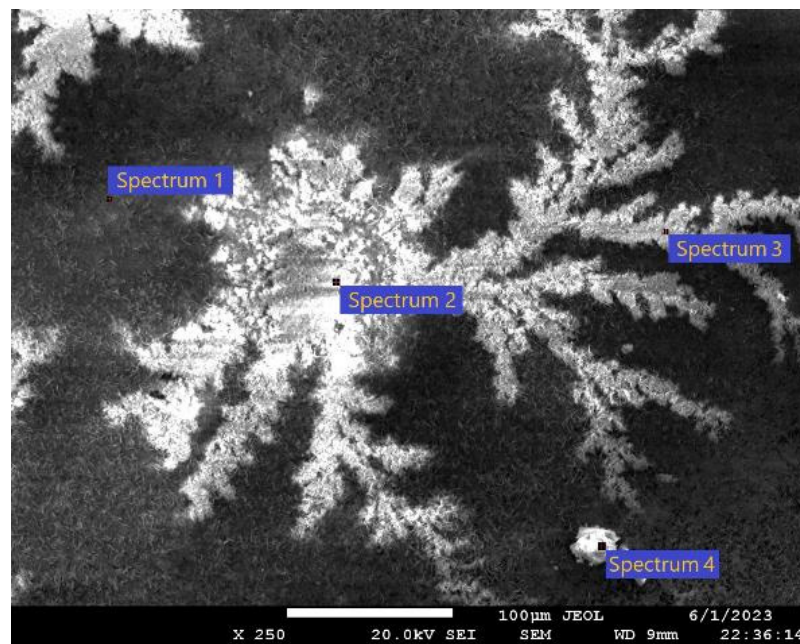


Figure 10. SEM-EDS analysis of degradation products of RS-treated Zn-1%Mg-0.1%Ca alloy.

Table 4. SEM-EDS analysis of degradation products of RS-treated Zn-1%Mg-0.1%Ca alloy (at. %).

Spectrum	Zn, %	O, %	Cl, %	K, %	Na, %	S, %	Ca, %	P, %	Total, %
Spectrum 1	31.85	60.74	6.36	0.72	-	0.33	-	-	100.00
Spectrum 2	4.22	6.37	44.07	0.23	45.11	-	-	-	100.00
Spectrum 3	3.42	11.59	38.71	-	46.28	-	-	-	100.00
Spectrum 4	33.51	61.26	4.37	0.38	-	0.27	0.21	~0.001	100.00

Since this work involved obtaining alloys that are promising for the development of implantable medical devices, the assessment of biocompatibility is a necessary aspect of studying the effect of RS on the original alloys. A comparative analysis of the effect of the Zn-1%Mg and Zn-1%Mg-0.1%Ca alloys before and after RS on hemolysis, cell viability, and cell colonization was conducted for this purpose.

The results of the assessment of induced hemolysis did not show a significant difference between the groups of samples in the initial and RS-treated states after 2 h of co-incubation with RBC (Table 5). It is a typical situation for biocompatible materials and alloys. This preliminary conclusion was later confirmed by the results of other experiments. It was shown that incubation with alloy samples for 24 h does not lead to a significant decrease in cell viability in comparison with the control. It indicates the absence of a cytotoxic effect for Zn-1%Mg and Zn-1%Mg-0.1%Ca alloys in the initial state and after RS. Comparison of data obtained for alloys before and after RS also confirmed the absence of differences in the effect of deformed and undeformed alloys on cells ($p > 0.05$). In general, it can be concluded that RS did not affect the biocompatibility of the Zn-1%Mg and Zn-1%Mg-0.1%Ca alloys.

However, in accordance with current trends, the planned design of the implant and the choice of material for it should ensure not only optimal mechanical functions and biocompatibility but also a favorable response of the cells and tissues of the patient's body. It is known that various types of implant treatment can modulate the adhesion, proliferation, and phenotypic expression of osteoblast cells [48]. To assess the effect of RS on biological activity, cell colonization of the surface of alloy samples was studied (Table 5, Figure 10). Since the alloys are being developed to create orthopedic implants, MMSCs with osteogenic potential as a cell model were used [49]. The obtained results showed that all

studied samples stimulate cell colonization by activating their adhesion and proliferation. At the same time, the comparative analysis does not reveal a significant effect of RS on this parameter of biological activity (Table 5, Figure 11). However, a trend towards an increase in the number of proliferating living cells adhered to the surface of the Zn–1%Mg alloy after RS in comparison with the samples in the initial state should be noted ($p > 0.05$). It can be seen that most of the cells are alive and functionally active, arranged in clusters on the surface of RS-treated samples, and have a large flattened body. It indicates a high reactivity of the cell culture.

Table 5. Results of biological studies of Zn–1%Mg and Zn–1%Mg–0.1%Ca alloys in the initial state and after RS (* difference between initial and RS-treated states, $p < 0.05$).

Parameter	State	Mean \pm SD, %	* p
Hemolysis	Zn–1%Mg	Initial	6.8 \pm 1.5
		RS at 200 °C	6.3 \pm 0.9
	Zn–1%Mg–0.1%Ca	Initial	5.7 \pm 1.7
		RS at 200 °C	5.9 \pm 1.5
Cell viability	Zn–1%Mg	Initial	99.4 \pm 0.9
		RS at 200 °C	99.3 \pm 2.0
	Zn–1%Mg–0.1%Ca	Initial	101.0 \pm 2.6
		RS at 200 °C	99.7 \pm 4.6
Cell colonization	Zn–1%Mg	Initial	21.0 \pm 6.9
		RS at 200 °C	24.4 \pm 9.9
	Zn–1%Mg–0.1%Ca	Initial	22.6 \pm 15.5
		RS at 200 °C	23.7 \pm 3.9

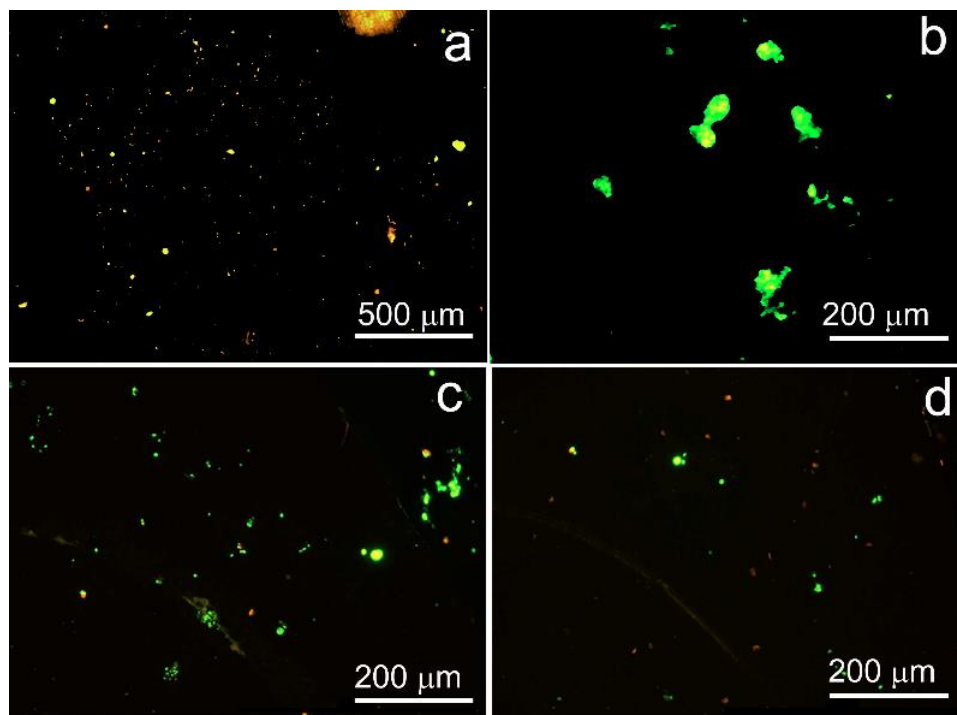


Figure 11. MMSCs on the surface of samples of studied alloys: (a)—Zn–1%Mg in the initial state, (b)—Zn–1%Mg after RS at 200 °C, (c)—Zn–1%Mg–0.1%Ca in the initial state, (d)—Zn–1%Mg–0.1%Ca after RS at 200 °C. Staining via two-color assay to determine live (green) and dead (red) cells.

Confirmed cell colonization stimulation via alloys is an important competitive advantage of the future implant. In particular, this property can help reduce the risk of developing implant-related infections since colonization of the implant surface using osteogenic cells is known to inhibit the formation of a bacterial film [50,51]. The maturation of cells follows after their adhesion and proliferation on the implant surface. At this stage, cells are characterized by an increased level of alkaline phosphatase activity, the synthesis of fibrillar collagen-I, and osteoid mineralization by hydroxyapatite [52,53]. Thus, the foundation is laid for the formation of a stable osteosynthesis that integrates the implant into the patient's bone tissue. This process provides a functional reconstruction for bone defects.

4. Conclusions

1. A partially recrystallized microstructure with an average size of recrystallized grains of 7 ± 0.4 and 10 ± 0.6 μm for Zn-1%Mg and Zn-1%Mg-0.1%Ca alloys, respectively, is formed in both studied alloys after rotary swaging at 200 °C. RS does not change the phase composition of the alloys but reduces the mass fraction of intermetallic phases.
2. RS significantly improves both the strength and ductility of the Zn-1%Mg and Zn-1%Mg-0.1%Ca alloys. It was possible to achieve a combination of UTS and elongation equal to 248 ± 9 MPa and $10.3 \pm 2.0\%$, respectively, in the Zn-1%Mg alloy after RS at 200 °C. In the case of the Zn-1%Mg-0.1%Ca alloy, these values were 246 ± 9 MPa and $14.2 \pm 0.9\%$, respectively.
3. The texture of the studied alloys changes slightly after RS at 200 °C.
4. RS at 200 °C does not affect the corrosion resistance (both chemical and electrochemical) of both studied alloys. The degradation rate of RS-treated Zn-1%Mg and Zn-1%Mg-0.1%Ca alloys was 0.28 ± 0.01 and 0.31 ± 0.03 mm/y, respectively, after 1 day of incubation in the complete growth medium. An increase in the incubation period slows down the degradation process due to the formation of a protective film. The rate of deceleration of the degradation process of the Zn-1%Mg alloy is greater than that of the Zn-1%Mg-0.1%Ca alloy.
5. RS does not impair the biocompatibility of the Zn-1%Mg and Zn-1%Mg-0.1%Ca alloys, maintaining the integrity of RBC and the viability of PBMC, providing adhesion and proliferation of osteogenic cells on the surface of samples.

Author Contributions: Conceptualization, N.M. and N.A.; methodology, M.K., A.K., and S.D.; software, N.M., N.A., G.R., V.S., M.Z., A.G., A.S., M.K., and V.Y.; validation, N.M., N.A., M.K., V.Y., and S.D.; formal analysis, N.M. and N.A.; investigation, N.M., N.A., G.R., O.R., V.S., M.Z., M.S., A.G., D.T., E.L., and A.S.; resources, M.K., V.Y., and S.D.; data curation, N.M., N.A., and A.K.; writing—original draft preparation, N.M. and N.A.; writing—review and editing, N.M., N.A., G.R., O.R., E.L., and A.K.; visualization, N.M. and N.A.; supervision, N.M., A.K., M.K., V.Y., and S.D.; project administration, N.M.; funding acquisition, N.M. All authors have read and agreed to the published version of the manuscript.

Funding: This research was supported by the Russian Science Foundation (Grant #22-13-00024).

Institutional Review Board Statement: The animal procedures and experiments with cells were assessed and approved by the Ethical Committee of the N.N. Blokhin NMRCO (protocol #05p-17/05/2023, approval date: 17 May 2023).

Informed Consent Statement: Not applicable.

Data Availability Statement: All the data required to reproduce these experiments are present in the article.

Acknowledgments: The studies of the surfaces of the samples after corrosion tests were performed using research equipment of the Shared Facility Center at P.N. Lebedev Physical Institute of the Russian Academy of Sciences.

Conflicts of Interest: The authors declare no conflict of interest.

References

1. Ageeva, L.I.; Alexandrova, G.A.; Golubev, N.A.; Kirillova, G.N.; Ohryzko, E.V.; Oskov, Y.I.; Nam, P.D.; Kharkov, T.L.; Chumarina, V.Z. *Health in Russia*; Statistical Collection; Rosstat: Moscow, Russia, 2021; p. 51. (In Russian)
2. Hussain, M.; Khan, S.M.; Al-Khaled, K.; Ayadi, M.; Abbas, N.; Chammam, W. Performance analysis of biodegradable materials for orthopedic applications. *Mater. Today Commun.* **2022**, *31*, 103167. [[CrossRef](#)]
3. Chandra, G.; Pandey, A. Biodegradable bone implants in orthopedic applications: A review. *Biocybern. Biomed. Eng.* **2020**, *40*, 596–610. [[CrossRef](#)]
4. Ekanayake, C.; Gamage, J.C.P.H.; Mendis, P.; Weerasinghe, P. Revolution in orthopedic immobilization materials: A comprehensive review. *Heliyon* **2023**, *9*, e13640. [[CrossRef](#)]
5. Salahshoor, M.; Guo, Y. Biodegradable orthopedic magnesium-calcium (MgCa) alloys, processing, and corrosion performance. *Materials* **2012**, *5*, 135–155. [[CrossRef](#)]
6. Roshal, L.M.; Lushnikov, A.M.; Basargin, D.Y.; Vorobev, D.A.; Nikishov, S.O. The use of biodegradable implants in the treatment of juxta- and intraarticular fractures in children. *Det. Khirurgiya (Russ. J. Pediatr. Surg.)* **2018**, *22*, 116–119. (In Russian) [[CrossRef](#)]
7. Yuan, W.; Xia, D.; Wu, S.; Zheng, Y.; Guan, Z.; Rau, J.V. A review on current research status of the surface modification of Zn-based biodegradable metals. *Bioact. Mater.* **2022**, *7*, 192–216. [[CrossRef](#)]
8. Li, G.; Yang, H.; Zheng, Y.; Chen, X.-H.; Yang, J.-A.; Zhu, D.; Ruan, L.; Takashima, K. Challenges in the use of zinc and its alloys as biodegradable metals: Perspective from biomechanical compatibility. *Acta Biomater.* **2019**, *97*, 23–45. [[CrossRef](#)]
9. Luqman, M.; Ali, Y.; Zaghoul, M.M.Y.; Sheikh, F.A.; Chan, V.; Abdal-hay, A. Grain refinement mechanism and its effect on mechanical properties and biodegradation behaviors of Zn alloys—A review. *J. Mater. Res. Technol.* **2023**, *24*, 7338–7365. [[CrossRef](#)]
10. Roohani, N.; Hurrell, R.; Kelishadi, R.; Schulin, R. Zinc and its importance for human health: An integrative review. *J. Res. Med. Sci.* **2013**, *18*, 144–157.
11. Hernández-Camacho, J.D.; Vicente-García, C.; Parsons, D.S.; Navas-Enamoradoc, I. Zinc at the crossroads of exercise and proteostasis. *Redox Biol.* **2020**, *35*, 101529. [[CrossRef](#)]
12. O'Connor, J.P.; Kanjilal, D.; Teitelbaum, M.; Lin, S.S.; Cottrell, J.A. Zinc as a Therapeutic Agent in Bone Regeneration. *Materials* **2020**, *13*, 2211. [[CrossRef](#)]
13. Tyszka-Czochara, M.; Grzywacz, A.; Gdula-Argasińska, J.; Librowski, T.; Wiliński, B.; Opoka, W. The role of zinc in the pathogenesis and treatment of central nervous system (CNS) diseases. Implications of zinc homeostasis for proper CNS function. *Acta Pol. Pharm.* **2014**, *71*, 369–377. [[PubMed](#)]
14. Shankar, A.H.; Prasad, A.S. Zinc and immune function: The biological basis of altered resistance to infection. *Am. J. Clin. Nutr.* **1998**, *68* (Suppl. 2), 447S–463S. [[CrossRef](#)]
15. Garner, T.B.; Hester, J.M.; Carothers, A.; Diaz, F.J. Role of zinc in female reproduction. *Biol. Reprod.* **2021**, *104*, 976–994. [[CrossRef](#)]
16. Prasad, A.S.; Mantzoros, C.S.; Beck, F.W.; Hess, J.W.; Brewer, G.J. Zinc status and serum testosterone levels of healthy adults. *Nutrition* **1996**, *12*, 344–348. [[CrossRef](#)]
17. Seo, H.J.; Cho, Y.E.; Kim, T.; Shin, H.I.; Kwun, I.S. Zinc may increase bone formation through stimulating cell proliferation, alkaline phosphatase activity and collagen synthesis in osteoblastic MC3T3-E1 cells. *Nutr. Res. Pract.* **2010**, *4*, 356–361. [[CrossRef](#)]
18. Murni, N.; Dambatta, M.; Yeap, S.; Froemming, G.R.A.; Hermawan, H. Cytotoxicity evaluation of biodegradable Zn–3Mg alloy toward normal human osteoblast cells. *Mater. Sci. Eng. C* **2015**, *49*, 560–566. [[CrossRef](#)]
19. Liu, Y.; Du, T.; Qiao, A.; Mu, Y.; Yang, H. Zinc-Based Biodegradable Materials for Orthopaedic Internal Fixation. *J. Funct. Biomater.* **2022**, *13*, 164. [[CrossRef](#)]
20. Tong, X.; Zhang, D.; Zhang, X.; Su, Y.; Shi, Z.; Wang, K.; Lin, J.; Li, Y.; Lin, J.; Wen, C. Microstructure, mechanical properties, biocompatibility, and in vitro corrosion and degradation behavior of a new Zn–5Ge alloy for biodegradable implant materials. *Acta Biomater.* **2018**, *82*, 197–204. [[CrossRef](#)]
21. Liu, S.; Doan, N.; Wang, G. Effect of Magnesium on Mechanical Properties of Binary Zn–Mg Alloys. In Proceedings of the 7th International Conference on the Development of Biomedical Engineering in Vietnam, Ho Chi Minh City, Vietnam, 27–29 June 2018; Springer: Singapore; Volume 69. [[CrossRef](#)]
22. Dambatta, M.S.; Izman, S.; Kurniawan, D.; Hermawan, H. Processing of Zn–3Mg alloy by equal channel angular pressing for biodegradable metal implants. *J. King Saud Univ. Sci.* **2017**, *29*, 455–461. [[CrossRef](#)]
23. Li, P.; Zhang, W.; Dai, J.; Xepapadeas, A.B.; Schweizer, E.; Alexander, D.; Scheideler, L.; Zhou, C.; Zhang, H.; Wan, G.; et al. Investigation of zinc-copper alloys as potential materials for craniomaxillofacial osteosynthesis implants. *Mater. Sci. Eng. C Mater. Biol. Appl.* **2019**, *103*, 109826. [[CrossRef](#)]
24. Huang, T.; Liu, Z.; Wu, D.; Yu, H. Microstructure, mechanical properties, and biodegradation response of the grain-refined Zn alloys for potential medical materials. *J. Mater. Res. Technol.* **2021**, *15*, 226–240. [[CrossRef](#)]
25. Werkhoven, R.J.; Sillekens, W.H.; van Lieshout, J.B.J.M. Processing Aspects of Magnesium Alloy Stent Tube. In *Magnesium Technology*; Sillekens, W.H., Agnew, S.R., Neelameggham, N.R., Mathaudhu, S.N., Eds.; Springer: Cham, Switzerland, 2011. [[CrossRef](#)]
26. Liu, Y.; Liu, J.; Herrmann, M.; Schenck, C.; Kuhfuss, B. Material Flow in Infeed Rotary Swaging of Tubes. *Materials* **2021**, *14*, 58. [[CrossRef](#)]

27. Trojanová, Z.; Drozd, Z.; Škraban, T.; Minárik, P.; Džugan, J.; Halmešová, K.; Németh, G.; Lukáč, P.; Chmelík, F. Effect of rotary swaging on microstructure and mechanical properties of an AZ31 magnesium alloy. *Adv. Eng. Mater.* **2020**, *22*, 1900596. [[CrossRef](#)]
28. Martynenko, N.; Anisimova, N.; Kiselevskiy, M.; Tabachkova, N.; Temralieva, D.; Prosvirnin, D.; Terentiev, V.; Koltygin, A.; Belov, V.; Morosov, M.; et al. Structure, mechanical characteristics, biodegradation, and in vitro cytotoxicity of magnesium alloy ZX11 processed by rotary swaging. *J. Magnes. Alloy* **2020**, *8*, 1038–1046. [[CrossRef](#)]
29. Huang, Z.; Liu, C.; Jiang, S.; Xiao, H.; Chen, X.; Wan, Y.; Zeng, G. Achieving high-strength nanocrystalline WE43 Mg alloy by a combination of cold rotary swaging and aging treatment. *Vacuum* **2022**, *197*, 110840. [[CrossRef](#)]
30. Minárik, P.; Zemková, M.; Král, R.; Mhaede, M.; Wagner, L.; Hadzima, B. Effect of microstructure on the corrosion resistance of the AE42 magnesium alloy processed by rotary swaging. *Acta Phys. Pol. A* **2015**, *128*, 805–807. [[CrossRef](#)]
31. Yang, Z.; Liu, C.; Gao, Y.; Guo, X.; Wan, Y. Enhanced mechanical and corrosion performance by forming micro shear bands in cold forged Mg-Gd-Y-Zr alloy. *Materials* **2020**, *13*, 3181. [[CrossRef](#)]
32. Martynenko, N.; Lukyanova, E.; Anisimova, N.; Kiselevskiy, M.; Serebryany, V.; Yurchenko, N.; Raab, G.; Birbilis, N.; Salishchev, G.; Dobatkin, S.; et al. Improving the property profile of a bioresorbable Mg-Y-Nd-Zr alloy by deformation treatments. *Materialia* **2020**, *13*, 100841. [[CrossRef](#)]
33. Ding, F.; Zhang, Y.; Zhu, X.; Guo, P.; Yang, L.; Zhang, Q.; Xu, C.; Sun, W.; Song, Z. Strengthening Mechanism of Rotary-Forged Deformable Biodegradable Zn-0.45Li Alloys. *Materials* **2023**, *16*, 3003. [[CrossRef](#)]
34. Estrin, Y.; Martynenko, N.; Lukyanova, E.; Serebryany, V.; Gorshenkov, M.; Morozov, M.; Yusupov, V.; Dobatkin, S. Effect of rotary swaging on microstructure, texture, and mechanical properties of a Mg-Al-Zn alloy. *Adv. Eng. Mater.* **2020**, *22*, 1900506. [[CrossRef](#)]
35. Savyolova, T.I.; Kourtasov, S.F. ODF restoration by orientation grid. *Mater. Sci. Forum* **2005**, *495*, 301–306. [[CrossRef](#)]
36. ASTM G59–97(2003); Standard Test Method for Conducting Potentiodynamic Polarization Resistance Measurements. ASTM International: West Conshohocken, PA, USA, 2006.
37. Sahu, B.P.; Sarangi, C.K.; Mitra, R. Effect of Zr content on structure property relations of Ni-Zr alloy thin films with mixed nanocrystalline and amorphous structure. *Thin Solid Film.* **2018**, *660*, 31–45. [[CrossRef](#)]
38. ASTM G31-21; Standard Guide for Laboratory Immersion Corrosion Testing of Metals. ASTM International: West Conshohocken, PA, USA, 2004.
39. Martynenko, N.; Anisimova, N.; Rybalchenko, O.; Kiselevskiy, M.; Rybalchenko, G.; Tabachkova, N.; Zheleznyi, M.; Prosvirnin, D.; Filonenko, D.; Bazhenov, V.; et al. Effect of high-pressure torsion on microstructure, mechanical and operational properties of Zn-1%Mg-0.1%Ca alloy. *Metals* **2022**, *12*, 1681. [[CrossRef](#)]
40. Martynenko, N.; Anisimova, N.; Rybalchenko, O.; Kiselevskiy, M.; Rybalchenko, G.; Tabachkova, N.; Zheleznyi, M.; Temralieva, D.; Bazhenov, V.; Koltygin, A.; et al. Structure, biodegradation, and in vitro bioactivity of Zn-1%Mg alloy strengthened by high-pressure torsion. *Materials* **2022**, *15*, 9073. [[CrossRef](#)]
41. Lou, D.; Wang, L.; Ren, Y.; Li, H.; Qin, G. Textural evolution and improved ductility in Zn-0.2Mg-0.8Mn (wt.%) alloys at different extrusion temperatures. *J. Alloys Compd.* **2021**, *860*, 158530. [[CrossRef](#)]
42. Wang, L.; Lou, D.; Ren, Y.; Qin, G.; Bai, P.; Zhao, Z. Effect of Mn content on the microstructure and mechanical properties of as-extruded Zn-0.2Mg-Mn (wt.%) alloys. *Mater. Character.* **2022**, *194*, 112400. [[CrossRef](#)]
43. Mollaei, N.; Fatemi, S.M.; Aboutalebi, M.R.; Razavi, S.H.; Bednarczyk, W. Dynamic recrystallization and deformation behavior of an extruded Zn-0.2 Mg biodegradable alloy. *J. Mater. Res. Technol.* **2022**, *19*, 4969–4985. [[CrossRef](#)]
44. Liu, S.; Zhan, H.; Kent, D.; Tan, Q.; Yin, Y.; Doan, N.; Wang, C.; Dargusch, M.; Wang, G. Effect of Mg on dynamic recrystallization of Zn-Mg alloys during room-temperature compression. *Mater. Sci. Eng. A* **2022**, *830*, 142243. [[CrossRef](#)]
45. Jarzębska, A.; Maj, Ł.; Bieda, M.; Chulist, R.; Wojtas, D.; Wątroba, M.; Janus, K.; Rogal, Ł.; Sztwiertnia, K. Dynamic Recrystallization and Its Effect on Superior Plasticity of Cold-Rolled Bioabsorbable Zinc-Copper Alloys. *Materials* **2021**, *14*, 3483. [[CrossRef](#)]
46. García-Mintegui, C.; Córdoba, L.C.; Buxadera-Palomero, J.; Marquina, A.; Jiménez-Piqué, E.; Ginebra, M.-P.; Cortina, J.L.; Pegueroles, M. Zn-Mg and Zn-Cu alloys for stenting applications: From nanoscale mechanical characterization to in vitro degradation and biocompatibility. *Bioact. Mater.* **2021**, *6*, 4430–4446. [[CrossRef](#)]
47. Hanawa, T.; Hiromoto, S.; Yamamoto, A.; Kuroda, D.; Asami, K. XPS Characterization of the Surface Oxide Film of 316L Stainless Steel Samples that were Located in Quasi-Biological Environments. *Mater. Trans.* **2002**, *43*, 3088–3092. [[CrossRef](#)]
48. Alves, S.F.; Wassall, T. In vitro evaluation of osteoblastic cell adhesion on machined osseointegrated implants. *Braz. Oral Res.* **2009**, *23*, 131–136. [[CrossRef](#)] [[PubMed](#)]
49. Dvorakova, J.; Wiesnerova, L.; Chocholata, P.; Kulda, V.; Landsmann, L.; Cedikova, M.; Kripnerova, M.; Eberlova, L.; Babuska, V. Human cells with osteogenic potential in bone tissue research. *BioMed. Eng. OnLine* **2023**, *22*, 33. [[CrossRef](#)]
50. Chu, L.; Yang, Y.; Yang, S.; Fan, Q.; Yu, Z.; Hu, X.L.; James, T.D.; He, X.P.; Tang, T. Preferential colonization of osteoblasts over co-cultured bacteria on a bifunctional biomaterial surface. *Front. Microbiol.* **2018**, *9*, 2219. [[CrossRef](#)]
51. Busscher, H.J.; van der Mei, H.C.; Subbiahdoss, G.; Jutte, P.C.; van den Dungen, J.J.; Zaat, S.A.; Schultz, M.J.; Grainger, D.W. Biomaterial-associated infection: Locating the finish line in the race for the surface. *Sci. Transl. Med.* **2012**, *4*, 153rv110. [[CrossRef](#)]

52. Sommer, K.P.; Krolinski, A.; Mirkhalaf, M.; Zreiqat, H.; Friedrich, O.; Vielreicher, M. Protocol for cell colonization and comprehensive monitoring of osteogenic differentiation in 3D scaffolds using biochemical assays and multiphoton imaging. *Int. J. Mol. Sci.* **2023**, *24*, 2999. [[CrossRef](#)]
53. Infante, A.; Rodríguez, C.I. Osteogenesis and aging: Lessons from mesenchymal stem cells. *Stem Cell Res. Ther.* **2018**, *9*, 244. [[CrossRef](#)]

Disclaimer/Publisher's Note: The statements, opinions and data contained in all publications are solely those of the individual author(s) and contributor(s) and not of MDPI and/or the editor(s). MDPI and/or the editor(s) disclaim responsibility for any injury to people or property resulting from any ideas, methods, instructions or products referred to in the content.